AugPrint: 3D Printing Foam Augmentations Directly Onto Objects Using Viscous Thread Printing

Jerry Cao
University of Washington
Seattle, Washington, USA
jcao22@cs.washington.edu

Yuecheng Peng
University of Washington
Seattle, Washington, USA
ychpeng@uw.edu

Hongrui Wu
University of Washington
Seattle, Washington, USA
hrwu@uw.edu

Yuxuan Miao
University of Washington
Seattle, Washington, USA
ymiao6@uw.edu

Sanjana Satagopan
University of Washington
Seattle, Washington, USA
ssatagop@uw.edu

Runxin Shi
University of Washington
Seattle, Washington, USA
rshi3@uw.edu

Brier Hehmeyer
The Overlake School
Redmond, Washington, USA
bmhehmeyer@gmail.com

Brett Emery
Northeastern University
Boston, Massachusetts, USA
emery.b@northeastern.edu

Jeffrey Lipton
Northeastern University
Boston, Massachusetts, USA
j.lipton@northeastern.edu

Richard Li
University of Washington
Seattle, Washington, USA
lichard@cs.washington.edu

Jennifer Mankoff
University of Washington
Seattle, Washington, USA
jmankoff@cs.washington.edu

Shwetak Patel
University of Washington
Seattle, Washington, USA
shwetak@cs.washington.edu

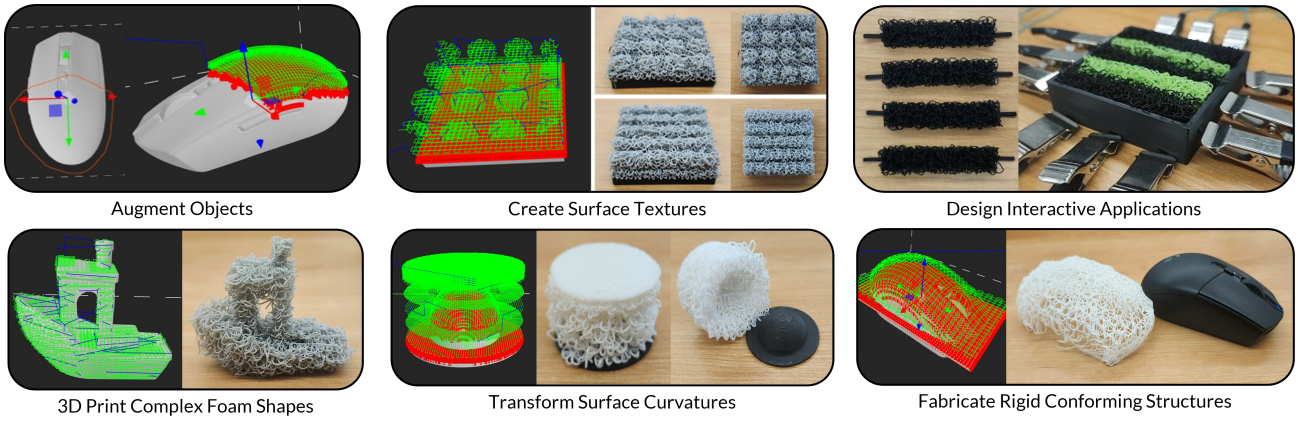


Figure 1: In AugPrint, we explore many different applications of viscous thread printing, including using it to augment objects, create surface textures, design interactive applications, 3D print complex foam structures, transform curved surfaces into flat surfaces, and fabricate rigid structures conforming to everyday objects.

Abstract

Combining soft-structure fabrication, direct-to-object augmentation, and embedded interactivity remains challenging, typically requiring specialized hardware, precise 3D scanning, or complex post-processing. AugPrint demonstrates how viscous thread printing (VTP) can bridge all three domains using an unmodified consumer-grade 3D printer. VTP leverages liquid rope coiling to deposit material from a high clearance, thereby inherently mitigating print-head collisions on curved surfaces. The extruded filament remains viscous enough to passively conform to underlying geometries without requiring precise mesh alignment. We present a design tool that enables users to create gradient-density foam augmentations on curved surfaces with non-planar toolpath generation, stiffness control, and surface texturing. We also establish the viability of embedded pressure sensing using commercially available conductive TPU printed with VTP. We demonstrate these capabilities through end-to-end applications, including a pressure-mapping bike seat and a shock-absorbing microcontroller enclosure.

This work is licensed under a Creative Commons Attribution 4.0 International License.

SCF '26, Tokyo, Japan

© 2026 Copyright held by the owner/author(s).

ACM ISBN 979-8-4007-2821-1/2026/12
https://doi.org/10.1145/3828611.3845659

CCS Concepts

• **Human-centered computing → Human computer interaction (HCI)**.

Keywords

3D printing, augmentation, viscous thread printing, liquid rope coiling

ACM Reference Format:

Jerry Cao, Yuecheng Peng, Hongrui Wu, Yuxuan Miao, Sanjana Satagopan, Runxin Shi, Brier Hehmeyer, Brett Emery, Jeffrey Lipton, Richard Li, Jennifer Mankoff, and Shwetak Patel. 2026. AugPrint: 3D Printing Foam Augmentations Directly Onto Objects Using Viscous Thread Printing. In *Proceedings of the 11th ACM Symposium on Computational Fabrication (SCF '26), December 06–08, 2026, Tokyo, Japan.* ACM, New York, NY, USA, 16 pages. https://doi.org/10.1145/3828611.3845659

1 Introduction

The frontier of personal fabrication is rapidly shifting from manufacturing standalone plastic artifacts to directly augmenting the physical world, a transition that relies on advancements across three critical domains. First, integrating existing physical objects into digital workflows offers profound practical advantages: it can reduce material waste and allow users to retain the highly refined shapes of the tools they already own [Chen et al. 2015, 2016; Mueller et al. 2014; Peng et al. 2018; Teibrich et al. 2015; Wall et al. 2021]. Second, fabricating soft structures allows researchers to move beyond rigid plastics, enabling tunable properties for personalized comfort and shock absorption [Martínez et al. 2016; Visser et al. 2019]. Finally, embedding interactivity transforms static artifacts into context-aware devices capable of capturing natural physical interactions [Child et al. 2026; Koyama et al. 2015; Ramakers et al. 2016]. Each of these domains has seen substantial progress on its own, but their intersection unlocks an entirely new design space. Bridging these domains would allow makers to retrofit tools they already own with tunable, ergonomic interfaces that capture physical interactions, such as seating posture or grip fatigue. However, combining these capabilities simultaneously without expensive, specialized multi-axis 3D printers, precise commercial-grade 3D scanners, and/or complex post-processing remains a significant challenge.

In this paper, we present AugPrint, which leverages viscous thread printing (VTP) to bridge this gap. Traditional 3D printing on existing objects, a necessary step for this intersection, is notoriously difficult due to imprecise surface meshes and print-head collisions. Fused filament fabrication (FFF) requires sub-millimeter surface leveling, which is incompatible with the millimeter-scale resolution of standard smartphone scans [Di Stefano et al. 2021]. Furthermore, navigating curved surfaces often causes the print head to collide with the object unless non-standard multi-axis printers [Peng et al. 2018] or extended nozzles [Liu et al. 2021] are used. VTP circumvents these issues by utilizing a fluid dynamics phenomenon known as liquid rope coiling (LRC) [Barnes and Woodcock 1958; Habibi et al. 2006; Maleki et al. 2004; Ribe 2004; Ribe et al. 2012]. Because VTP deposits material from a high clearance, it inherently avoids print-head collisions on high-curvature surfaces. Simultaneously, the extruded filament remains sufficiently viscous to passively drape and conform to underlying objects, reducing the need for precise mesh alignment.

Beyond simply conforming to existing geometries, VTP's deposition mechanics are inherently compatible with fabricating soft, functional structures. Unlike traditional methods that require complex 3D lattice generation to achieve compliance, VTP natively produces highly compressible, foam-like structures. By dynamically tuning parameters such as print height, extrusion speed, and toolpath velocity, AugPrint allows users to locally modulate the foam's porosity and stiffness [Emery et al. 2024; Lipton and Lipson 2016], making it well-suited for creating custom ergonomic padding. Furthermore, this porous architecture serves as an ideal substrate for embedded interactivity. When printed using commercially available conductive elastomers, these tunable foams function as piezoresistive pressure sensors. Crucially, because these structural and functional variations are controlled entirely by adjusting toolpath parameters rather than swapping hardware, custom padding and integrated sensors can be fabricated simultaneously while the nozzle safely navigates the object's curvature. While foams produced via VTP exhibit weaker interlayer adhesion compared to solid prints, prior work has demonstrated that they are highly durable for applications where forces are predominantly compressive [Miske et al. 2025; Willemstein et al. 2025, 2024].

In AugPrint, we showcase the unique strengths of this approach by enabling the design and fabrication of soft, interactive foams directly onto existing objects using unmodified consumer-grade 3D printers. We first detail our computational design tool, which abstracts the complex fluid dynamics of LRC to enable non-planar toolpath generation, gradient stiffness control, and surface texturing. We then demonstrate how AugPrint facilitates traditional fabrication approaches, using VTP foam as support material that levels highly curved surfaces for conventional FFF printing. Finally, we establish the viability of using commercially available conductive TPU to create embedded LRC pressure sensors, culminating in end-to-end practical applications, including a custom-fit, pressure-mapping bike seat and a shock-absorbing microcontroller enclosure.

The contributions of this paper are threefold: (1) exploring VTP for printing directly onto existing curved geometries; (2) introducing non-planar chunk-based slicing for VTP to increase printability; (3) demonstrating and characterizing consumer-grade conductive TPU foams for sensing.

2 Related Work

AugPrint draws on advances across three research areas: integrating existing physical objects into fabrication workflows, 3D printing soft and mechanically tunable structures, and embedding interactivity into fabricated artifacts. Each area has matured considerably on its own, producing techniques that range from printing directly on surfaces to creating lattice-based compliant mechanisms to embedding conductive traces for touch sensing. However, each area also imposes characteristic constraints, such as requiring precise meshes, specialized printers, or complex post-processing, that compound when combining areas. No existing approach simultaneously deposits soft, conformal, and interactive material onto an existing object using consumer-grade hardware. To situate AugPrint within

Table 1: Comparison of fabrication techniques for augmenting physical objects.

Work	Low-Fi Meshes	Standard Printer	Easy Post-Processing	High Curvature	Direct on Object
AugPrint (ours)	✓	✓	✓	✓	✓
RoMA [Peng et al. 2018]	✓		✓	✓	✓
RetroFab [Ramakers et al. 2016]	✓	✓		✓	
ShrinCage [Sun et al. 2021]	✓	✓	✓		
CopyCAD [Follmer et al. 2010]			✓		
Reprise [Chen et al. 2016]		✓	✓		
Encore [Chen et al. 2015]		✓			✓
ReForm [Weichel et al. 2015]		✓	✓		✓
Patching [Teibrich et al. 2015]			✓		✓
Augmented Fab [Ashbrook et al. 2016]		✓	✓		
Robiot [Li et al. 2019]		✓	✓	✓	
Roman [Li et al. 2022]		✓		✓	
AutoConnect [Koyama et al. 2015]		✓	✓	✓	
Facade [Guo et al. 2017]		✓	✓		
faBrickation [Mueller et al. 2014]		✓			
Medley [Chen et al. 2018]		✓	✓	✓	
Scrappy [Wall et al. 2021]		✓	✓		
Substiports [Wall et al. 2023]		✓	✓		✓
Printegrated [Child et al. 2026]		✓	✓	✓	
GyFoam [Wang et al. 2025]		✓		✓	

this landscape, we survey each domain and provide background on viscous thread printing, the technique that enables AugPrint to span all three domains.

2.1 Integrating Existing Objects Within Fabrication Workflows

Researchers have pursued a range of technical strategies to bring existing physical objects into digital fabrication pipelines. Several systems print directly onto object surfaces [Peng et al. 2018; Teibrich et al. 2015; Weichel et al. 2015], while others use heat-shrinkable materials that conform to objects post-fabrication [Sun et al. 2021; Wang et al. 2025]. A complementary line of work leverages existing artifacts as structural infill or support material to reduce waste [Mueller et al. 2014; Wall et al. 2021, 2023]. The motivating goals across these approaches span accessibility and assistive augmentation [Chen et al. 2015, 2016; Guo et al. 2017], rapid prototyping [Follmer et al. 2010; Mueller et al. 2014], embedded sensing [Koyama et al. 2015; Ramakers et al. 2016], electronics integration [Child et al. 2026], and attachment of new functional components [Li et al. 2019, 2022]. However, as shown in Table 1, each approach involves significant practical tradeoffs. Many require high-fidelity object meshes beyond what a smartphone scanner can provide [Di Stefano et al. 2021], involve difficult post-processing such as manual assembly or surface finishing, or necessitate non-standard fabrication equipment, such as the multi-axis robotic setup in RoMA [Peng et al. 2018]. Furthermore, the vast majority of these systems deposit rigid thermoplastics, meaning that even when augmentation succeeds, the result is a hard attachment rather than a soft, ergonomic interface. As a result, while the conceptual benefits of augmenting physical objects are well established, simultaneously achieving conformal deposition, mechanical compliance, and accessibility on consumer hardware remains unresolved.

2.2 Approaches to 3D Printing Soft Structures

While soft structures can also be fabricated through textiles or casting, 3D printing offers a continuously tunable stiffness range within a single part, freeform volumetric geometry that sheet-based and mold-based processes cannot easily produce, and a direct, tool-free path from a digital model to a physical part on consumer hardware. Besides VTP, two popular methods for 3D printing soft structures are (1) constructing lattice geometries, and (2) using foaming materials. Both produce mechanically robust results, but each imposes constraints on the range of achievable structures.

Foaming materials rely on chemical blowing agents or physical porogen inclusions to create porosity, typically limiting volume expansion to 100–300% of the original filament volume [Nofar et al. 2022]. This constrains the range of producible pore sizes and, consequently, the stiffnesses that can be achieved [Silverstein 2014; Visser et al. 2019]. Lattice geometries offer more geometric control in principle, but require a printer resolution finer than a unit cell by roughly an order of magnitude [Chu et al. 2008; Gibson et al. 2020; Martínez et al. 2016], and their fabrication demands extensive travel and retraction movements that increase the likelihood of print failure [Guerra Silva et al. 2021; Prajapati et al. 2022; Robles-Lorite et al. 2025]. Both approaches also share a limited ability to produce smooth stiffness gradients, a capability that VTP supports natively through continuous parameter modulation [Emery et al. 2024]. Other fabrication methods for soft structures exist—such as direct foam writing and direct bubble writing—but these require syringe-based printers and custom material formulations, rather than consumer FFF hardware [Muth et al. 2017; Visser et al. 2019].

Critically, these soft-structure techniques have been developed almost exclusively for standalone fabrication on flat build plates.

Adapting them to print on existing curved objects would reintroduce the mesh-precision and collision-avoidance challenges described above, a combination that none of these methods were designed to handle.

2.3 3D Printing Interactive Objects

Recent advances in additive manufacturing have enabled the transformation of static 3D-printed objects into interactive, sensor-integrated systems. These developments generally follow three dominant approaches: (1) leveraging geometric deformations to change resistance or capacitance, (2) embedding rigid conductive traces for touch sensing, and (3) employing post-processing techniques to add interactivity to finished geometries.

A significant body of work focuses on leveraging the deformation of 3D-printed geometries to sense physical interaction. Fluxable [Lee et al. 2024] utilizes helix-and-lattice designs to create deformable structures, integrating shape-memory alloys for both sensing and actuation. Similarly, MetaSense [Gong et al. 2021] embeds shear sensing within mechanical metamaterials, while FlexKeys [Greenspan et al. 2022] uses multi-material printing to create deformable springs for capacitive input. To streamline fabrication, Aguilar-Segovia et al. [2024] designed compact torque sensors in which the capacitive structures serve as both deformable and sensing elements. Further exploring material properties, Sakura et al. [2023, 2022] utilized conductive TPU lattices for pressure sensing, using non-conductive internal channels for wire routing. AcceloPrint [Ozbek et al. 2024, 2025] monitors acceleration via a 3D-printed apparatus based on the distance between a swinging conductive-PLA mass and a sensing plate.

A second approach embeds rigid touch-sensitive regions using conductive filaments printed during fabrication [Burstyn et al. 2015; He et al. 2021; Sakura and Kakehi 2025; Schmitz et al. 2015]. Variants of this strategy route conductive traces to interface with external sensors, such as capacitive touchscreens [Kato et al. 2020; Schmitz et al. 2021, 2017], or encode conductive patterns for authentication [Marky et al. 2020].

When direct printing is insufficient, researchers have proposed post-processing steps with conductive tape or inks to expand the functionality of 3D-printed objects. Early works such as Midas [Savage et al. 2012] and SurfCuit [Umetani and Schmidt 2017] involve attaching copper tape to printed surfaces to create circuits. Other methods incorporate fluidics, such as A Series of Tubes [Savage et al. 2014], which uses conductive liquids, or Off-Line Sensing [Schmitz et al. 2018], which integrates liquid-filled channels for sensing. More recently, Sprayable User Interfaces [Wessely et al. 2020] have demonstrated that conductive inks can be applied to complex printed surfaces to add sensing capabilities after printing.

While these techniques have produced increasingly sophisticated interactive objects, they have been developed primarily for standalone artifacts printed from scratch. Adapting them to augment existing objects would require solving the mesh-precision and collision-avoidance problems discussed in Section 2.1. Moreover, the rigid substrates and precise geometries on which most of these sensing approaches depend are fundamentally at odds with the soft, conformal structures needed for ergonomic augmentation—highlighting a tension between the interactivity and soft-structure domains that few existing systems attempt to reconcile.

2.4 Viscous Thread Printing Behavior and Applications

To address the challenges of soft-structure fabrication, direct augmentation, and embedded sensing simultaneously, we turn to viscous thread printing (VTP). At the core of VTP is liquid rope coiling (LRC), a fluid dynamics phenomenon that occurs when a viscous material is extruded from a sufficient height, causing the falling filament to become unstable and form characteristic coiled or helical patterns due to the combined effects of viscosity, gravity, and inertia [Barnes and Woodcock 1958; Habibi et al. 2006; Maleki et al. 2004; Ribe 2004; Ribe et al. 2012]. To better understand this phenomenon, researchers have developed mathematical models calculating coiling parameters in 2D space (e.g., period length, width, loop length) based on material extrusion settings such as back pressure, nozzle speed, diameter, and height [Ma et al. 2023; Tian et al. 2017]. Researchers have also extended this work to 3D, characterizing how coils behave when deposited on top of one another during the VTP process, enabling the prediction of structural properties, such as layer height and mechanical stiffness [Emery et al. 2021, 2024; Lipton and Lipson 2016]. Earlier work from our team has also examined the initial feasibility of printing on top of existing objects using VTP [Cao et al. 2026].

In Figure 2, we show their equations for V^* and H^*, two variables that govern coiling behavior in VTP. V^* is inversely proportional to coil density and is defined as the ratio between the print-head movement velocity and the filament extrusion velocity. H^* is directly proportional to coil diameter and is defined as the ratio between the height of the print head above the print surface and the diameter of the extruded filament. Then, for a distance ΔL between toolpaths within the same layer, the layer height ΔZ can be predicted using the predictive models of Emery et al. for the materials in their catalog (PLA and NinjaFlex 85A TPU) [Emery et al. 2024].

$$V^* = \frac{V}{C} \propto \frac{1}{\text{coil density}} \qquad H^* = \frac{H}{\alpha D_n} = \frac{H}{D_t} \propto \text{coil diameter}$$

Parameter	Definition
V	Print-head velocity (mm/s)
C	Filament extrusion velocity out of nozzle (mm/s)
H	Nozzle height above the print surface (mm)
D_n	Nozzle diameter (mm)
α	Swelling factor of filament after extrusion
D_t	Filament thread diameter after extrusion (mm)
ΔZ	Z increment per layer (mm)
ΔL	Distance between toolpaths in the same layer (mm)

Figure 2: Coiling behavior equations and parameter definitions for viscous thread printing (VTP).

Leveraging this predictability, researchers have explored VTP for various engineering applications, including the creation of living hinges, tailored insole orthotics, and soft robotic manipulators. Emery et al. interpolated printing parameters to create stiffness

gradients supporting stiffnesses from 10 to 400 kPa when printing with 85A TPU [Emery et al. 2024; Nakura et al. 2024], while Miske et al. demonstrated the viability of these foams for long-term use through extensive compression, shear, and flexural durability testing [Miske et al. 2025]. Researchers have also 3D-printed pressure and strain sensors using VTP. Willemstein et al. characterized the hysteresis, performance degradation, and structural durability of VTP sensors, showing they remained functional after 16,000 cycles when loaded to 500 N [Willemstein et al. 2025, 2024]. Beyond functional engineering, LRC has also been leveraged for creative expression by dynamically adjusting print parameters to create novel textures using materials like glass [Klein et al. 2015], clay [Mansoori et al. 2018], food [Alberts et al. 2024; Ghorbani et al. 2024], thermoplastics [Subbaraman and Peek 2024; Takahashi and Miyashita 2017], and elastomers [Alberts et al. 2024; Subbaraman et al. 2025].

However, current applications and models primarily target flat or 2.5D structures under constrained parameters, leaving several critical gaps. First, VTP extrusion behavior on highly curved 3D geometries remains unexplored. Second, extremely high H^* values are ignored since they are unnecessary for 2.5D printing. Finally, compatible functional materials are limited; for instance, Willemstein et al. used an inaccessible conductive TPE pellet (Shore 70A) [KRAIBURG TPE 2026], leaving consumer-grade conductive TPUs (Shore 90A–95A [Aloqalaa 2022]) unexplored. Furthermore, prior sensing applications rely on unidirectional toolpaths, restricting structural complexity.

Across the domains of soft structures, direct-to-object augmentation, and interactive fabrication, a consistent gap emerges: no existing approach simultaneously supports all three without requiring high-end equipment, precise object meshes, or complex post-processing. The fundamental fluid dynamics of VTP position it as a unique candidate to bridge these domains. Because VTP deposits material from a high clearance (H^*), it inherently avoids the print-head collisions that typically plague direct-to-object printing on high-curvature surfaces. Simultaneously, the extruded filament retains sufficient viscosity to passively drape and conform to underlying objects, relaxing the need for sub-millimeter scanning accuracy. Furthermore, by dynamically tuning the coil density (V^*), VTP can locally modulate the output structure's porosity and stiffness, providing an ideal, highly compressible substrate for embedded piezoresistive sensing. AugPrint builds on this theoretical foundation to enable direct-to-object fabrication with an unmodified consumer-grade printer, a capability that, as Table 1 shows, no prior system provides alongside soft, conformal deposition.

3 AugPrint System Overview

AugPrint is an end-to-end system for depositing soft, conformal foam onto existing objects using an unmodified consumer-grade FFF printer. Consider a user who wants to add a custom cushion to a bike seat. They begin with a smartphone scan of the seat, which they load into the AugPrint design tool. The tool identifies the augmentable surface, computes the nozzle clearance H^* required to traverse the seat's curvature without collision, and lets the user lasso the region to be padded. The user then uploads a grayscale SVG density map, created in any vector editor, so that the padding is softer where the rider's sit bones contact the seat and firmer at the edges for lateral support. AugPrint then translates these choices into VTP parameters (V^*, H^*, ΔL) that set the local porosity and stiffness of the deposited foam. Slicing produces a non-planar toolpath that follows the seat's geometry, together with a positioning outline that the user prints first to register the physical object on the build plate.

Three properties of viscous thread printing make this workflow possible on stock hardware. Depositing from a clearance of many nozzle diameters sidesteps the collision problem that otherwise forces multi-axis printers or extended nozzles. Because the extruded thread is still soft when it lands, it drapes onto the underlying surface; together with the high clearance, this relaxes the sub-millimeter scan accuracy required by conventional direct-to-object printing. And because stiffness is controlled by toolpath parameters rather than by hardware or material changes, a single continuous print can span the full range from compliant padding to firm support.

The same mechanism supports embedded sensing. By printing in conductive TPU, we can create pressure sensors. On a single-extruder printer, this simply requires changing the material. The remainder of the paper details the design tool (Section 5), evaluates tolerance to scan error (Section 6), characterizes the foam as a pressure sensor (Section 7), and demonstrates the system on four applications (Section 8).

4 AugPrint Design Tool Overview

To make VTP practical for direct-to-object fabrication and for creating complex soft structures, we built the AugPrint design tool. The tool translates the predictive models of liquid rope coiling described in Section 2.4 into an interactive design environment where users spatially assign VTP parameters—V^* and H^*—to control the local density and stiffness of printed foam. The tool supports two primary interaction modes: printing a standalone mesh and augmenting an existing object. In this section, we describe the user-facing pipeline for each mode; technical implementation details follow in Section 5.

In both modes, users can define VTP parameters globally or map them spatially using an uploaded SVG grayscale map. The tool applies a linear mapping from shade to density, where lighter shades correspond to denser, stiffer regions and darker shades to more porous, compliant regions. This gives users granular control over the mechanical properties of the final structure.

4.1 Printing a Standalone Mesh

To fabricate a standalone soft structure, users upload a 3D mesh into the design tool, assign VTP parameters (uniformly or via an SVG grayscale map), and slice. This mode functions similarly to a traditional slicer workflow but produces foam structures with tunable density rather than solid infill. The tool generates planar toolpaths and outputs the corresponding G-code.

4.2 Augmenting an Existing Object

Augmenting a physical object is more involved because the generated toolpath must conform to the object's surface curvature. Rather than slicing into flat horizontal layers, the tool generates non-planar

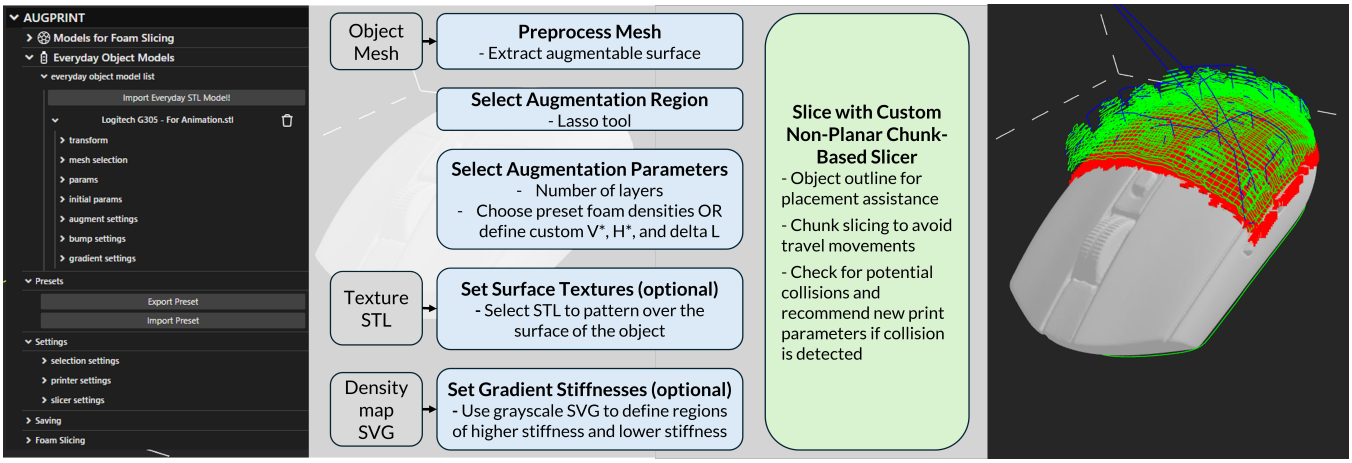


Figure 3: A system diagram for AugPrint's design tool showing the interface and the steps to augment an object.

toolpaths that follow the object's geometry. This non-planar approach offers two advantages over stacked planar layers. First, it produces a continuous curved outer shell on the augmentation's boundary; because intralayer adhesion in VTP structures is stronger than interlayer adhesion [Emery et al. 2021], this continuity significantly improves structural durability. Second, it eliminates the staircase artifacts that occur when approximating a curved surface with flat layers, yielding a smoother outer surface.

However, realizing these benefits on curved surfaces introduces fabrication constraints that do not arise in conventional planar printing. Because VTP relies on continuous deposition from a fixed height above the target surface, the print head cannot lift and reposition without leaving unwanted filament strands. Additionally, when printing on an object, the print head or its gantry may collide with it if the print height is set incorrectly. The design tool abstracts the constraints of continuous extrusion management, collision avoidance, and travel movement minimization (Figure 3). To use the design tool, users can perform the following:

1. **Upload and Analyze:** Users place a mesh of their object on the virtual build plate. The tool automatically identifies the augmentable surface and calculates the minimum H^* needed to safely clear the object without nozzle collisions.
2. **Define Augmentation Region and Thickness:** Using a lasso tool, users select the specific regions they wish to augment and specify the number of foam layers, which determines the thickness of the augmentation.
3. **Apply Surface Textures and Contours:** Users can apply geometric surface patterns (e.g., hemispherical bumps for grips) or define a target surface contour for the augmentation. In many applications, the desired top surface differs substantially from the bottom surface. When printing on a curved object, a user may want a flat top surface—for instance, to create a level platform for traditional 3D printing (Figure 1). Conversely, when printing on a flat build plate, a user may want a curved top surface to create an ergonomic contour. Users can specify these target contours by uploading an STL file that defines the desired surface shape.
4. **Map VTP Parameters:** Users assign V^* and H^* values for the augmentation, either uniformly or with an SVG gradient map.
5. **Position and Slice:** To help align the physical object on the real-world build plate, the tool generates positioning outlines (either top-down projections or interfacing cross-sections). The tool then slices the augmentation and generates G-code.

5 Design Tool Implementation

This section describes the technical implementation of the key features introduced in the design tool overview: generating non-planar toolpaths that conform to object surfaces, minimizing travel movements during printing, and modifying the surface geometry of augmentations through textures and gradients.

5.1 Non-Planar Toolpath Generation

To generate a non-planar toolpath that follows the contour of a target mesh, we first sample the mesh surface by casting rays downward from a plane positioned above the mesh's maximum height. These rays are arranged in a uniform rectilinear grid with spacing ΔL and oriented orthogonally to the XY plane. At each grid point, only the topmost intersection with the mesh is kept, producing a set of surface coordinates that define the augmentable region—the same surface shown during the Upload and Analyze step of the design tool (Section 4.2).

Adjacent surface coordinates are then connected to form a rectilinear toolpath, following the established convention for structural VTP printing [Emery et al. 2024; Willemstein et al. 2024]. To improve structural integrity, we rotate the deposition direction by 90° between layers by sorting grid points by (x, y) on one layer and (y, x) on the next, crosshatching the deposited filaments. The toolpath begins at one corner of the first layer, and subsequent layers start at whichever corner minimizes the travel distance from the previous layer's endpoint.

We adopt rectilinear toolpathing because VTP extrusion behavior has been characterized and validated in this context, and we use parameter combinations characterized by Emery et al. [2024] for the materials in our demonstrations (PLA and NinjaFlex 85A TPU). To handle transitions between disjoint meshes and separate closed regions, we draw on prior work in travel movement optimization

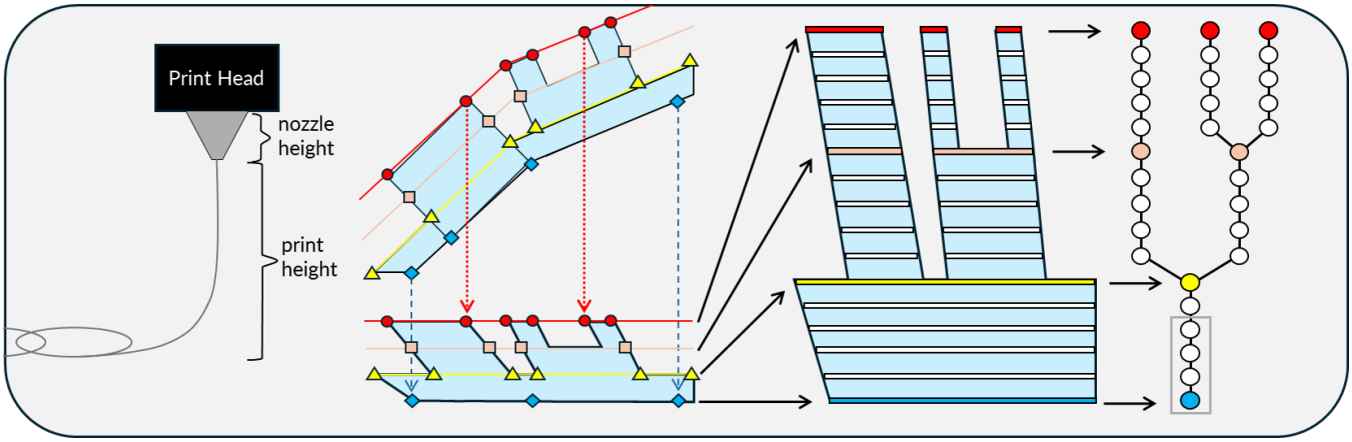


Figure 4: Visualization of the modified TRAvel Slicer algorithm from Section 5.2.2. First, note that our chunk height from the deposited surface equals the nozzle height plus the print height. Next, we project from a curved toolpath to a planar toolpath. Finally, using all the projected toolpaths, we construct our own height-dependency tree to determine the printing order. Each rectangle/dot represents a print layer. These layers are then grouped for printing in chunk heights.

to suppress unwanted print artifacts arising from LRC extrusion, as described in the following subsection.

5.2 Chunk-Based Slicing for Travel Reduction

VTP's continuous deposition makes standard travel movements problematic: filament continues to flow after extrusion ceases, producing unwanted strands when the print head repositions. Minimizing these travel movements is therefore critical to print quality. We address this by extending the open-source TRAvel Slicer by Gould et al. [2024] to support non-planar toolpaths with variable layer heights. First, we summarize key points of the original algorithm.

5.2.1 Background: The TRAvel Slicer Algorithm. TRAvel Slicer minimizes two types of travel movements: *Inner-Model* travel, which occurs within a single contiguous region of a layer, and *Outer-Model* travel, which occurs when the print head moves between separate regions or layers of the model. Because our VTP toolpaths use rectilinear infill (Section 5.1) to leverage existing VTP characterizations rather than TRAvel Slicer's inner-model toolpathing, we focus exclusively on its Outer-Model travel reduction strategy.

To reduce Outer-Model travel, TRAvel Slicer first slices the model into planar layers and identifies isolated regions at each layer height. It then constructs a *height-dependency tree*, where each node represents a closed region in a planar slice of the model. This tree captures the constraint that a child region cannot be printed before its parent, since it would have no surface to deposit onto.

Using this dependency tree, the TRAvel Slicer algorithm groups connected nodes into *chunks*—sequences of layers within a localized spatial region that are printed consecutively before the print head repositions. Each chunk is constrained to have a maximum height equal to the nozzle height, i.e., the distance the nozzle tip protrudes below the print-head body. For planar deposition, this constraint helps ensure that a print head can print in an adjacent chunk without colliding with previously deposited material. The algorithm then builds a directed weighted graph over these chunks, where edge weights correspond to the travel distance between chunk endpoints, and searches for a minimum-weight path that respects the dependency tree's parent-before-child ordering. By deferring repositioning until a vertical chunk is complete, this approach dramatically reduces the number of Outer-Model travel movements.

The full algorithm includes additional constraints to ensure collision-free printing between chunks, such as safe inter-chunk travel trajectories and ordering rules for chunks at the same height; we refer the reader to Gould et al. [2024] for complete implementation details. Here, we have summarized the aspects of the algorithm most relevant to our non-planar extension.

5.2.2 Extending TRAvel Slicer for Non-Planar Toolpaths. TRAvel Slicer was designed for planar layers on a flat build plate. To apply it to our non-planar toolpaths, we make two key adaptations: a modified chunk-height constraint that exploits VTP's elevated deposition clearance, and a planar-projection strategy to conform to the required input format for TRAvel Slicer (Figure 4).

In the original algorithm, the maximum chunk height is set to the nozzle height, since in conventional 3D printing, the nozzle nearly contacts the print surface, and any previously deposited material taller than the nozzle height risks colliding with the print-head body. In VTP, however, the nozzle deposits material from a substantial print height H above the surface (governed by H^*). The print-head body therefore sits at the nozzle height plus the print height above the layer being printed, and collisions with adjacent material occur only when that material exceeds this combined height. We therefore set the maximum chunk height to the nozzle height plus the print height, allowing significantly taller chunks than the original algorithm would permit. This reduces the total number of chunks and, consequently, the number of inter-chunk travel movements.

To handle the non-planar geometry, we use a planar projection strategy (Figure 4). We first project each non-planar slice obtained from mesh sampling (Section 5.1) onto a flat plane, discarding the z-coordinates. These flattened points serve as input to TRAvel Slicer's dependency-tree construction and chunk-ordering pipeline,

which operates on planar geometry. Once the algorithm produces a 2D toolpath with optimized chunk ordering, we restore each waypoint's z-coordinate by reprojecting it onto the original mesh surface. In effect, the chunk layout and ordering are computed as though the surface were flat, and then conformed to the true 3D geometry afterward.

Two additional steps ensure that the reprojected toolpath remains collision-free. First, between distant waypoints, the straight-line 2D path may cross regions where the surface rises sharply. We insert intermediate points at regular intervals along these segments before reprojection, so the resulting 3D toolpath closely follows the surface curvature rather than cutting through it. Second, after reprojection, we perform collision detection between the toolpath and the mesh geometry. Where violations are found, such as when a chunk's accumulated height would cause the print head to collide with a neighboring chunk, we subdivide the offending chunk into smaller vertical sections to resolve the conflict.

5.3 Surface Geometry Modifications

The design tool supports two forms of surface geometry modification: patterned textures and gradient surfaces.

Surface Textures. Users may upload an STL of a geometric primitive—such as a hemisphere for dot patterns or a rectangular prism for grooves (Section 4.2)—to be tiled across the augmentation surface. For each sample point on the target mesh, the tool computes the surface normal, aligns the base of the texture primitive to the tangent plane at that point, and projects the primitive onto the surface. Textures are tiled at the toolpath grid spacing ΔL. If part of a patterned mesh is generated outside the augmentable region, a boolean operation is performed to subdivide the mesh, preserving any printable regions. Texture geometry is unconstrained, so printability cannot be guaranteed for textures with large overhangs, as we do not natively support generating support structures.

Gradient Surfaces. To bridge between arbitrary bottom and top surface geometries (Section 4.2), the tool linearly interpolates between the two surfaces across the specified number of layers, producing a per-point target z-coordinate for each intermediate layer at each grid sample point. The required ΔZ at each point determines the necessary VTP parameters (H^* and V^* for a given ΔL). We select the closest-matching entry from a table of characterized VTP parameter combinations (H^*, V^*, ΔL, and the resulting ΔZ) for PLA and NinjaFlex 85A TPU from Emery et al. [2024]. So that our results can be reproduced without access to the full predictive model, the supplementary material lists every parameter combination used in this paper and the complete print settings for each artifact. The parameter table spans a range of layer heights for each material and ΔL.

When gradient-surface interpolation requests a ΔZ outside this range—for example, where the top and bottom surfaces diverge too sharply for the chosen number of layers—the nearest-match lookup clamps to the closest available entry, so the printed contour deviates from the target in those regions. Users can avoid out-of-range increments by increasing the number of layers. Separately, if a parameter assignment implies an H^* below the minimum collision-free clearance computed during Upload and Analyze, the slicer's collision check detects the conflict and recommends new print parameters (Figure 3). The current tool does not explicitly flag points where ΔZ was clamped; automatically selecting the number of layers and highlighting clamped regions in the preview are planned improvements.

5.4 Applying Planar Coiling Models to Curved Surfaces

The parameter combinations we use [Emery et al. 2024] were characterized for planar layers on flat substrates, so applying them to non-planar toolpaths assumes that coils accumulate on a curved surface as they would on a flat one. Three factors make this assumption approximate. First, because our toolpath grid is uniform in XY (Section 5.1), the spacing between adjacent passes measured along a surface inclined at angle θ is $\Delta L/\cos\theta$, so steep regions receive sparser foam than flat regions with the same nominal parameters. Second, H is measured vertically, so the standoff along the surface normal is approximately $H\cos\theta$, and the thread lands on a sloped surface, elongating the coil footprint downslope. Third, on steep slopes gravity has a tangential component that can pull still-viscous coils downslope, while concave regions can collect material from their surroundings; both effects redistribute foam relative to the flat-substrate prediction.

We did not systematically measure ΔZ on curved substrates in this work. Qualitatively, we observed that discrepancies were damped rather than compounded across successive layers, owing to the self-stabilizing behavior of VTP [Emery et al. 2024]. The local density of the final foam may nonetheless differ from the target. Characterizing coil accumulation on inclined and curved substrates, and compensating for slope by scaling ΔL with $\cos\theta$, are directions for future work.

6 Scanned Mesh Noise Tolerance Characterization

A practical limitation of any object augmentation technique is dependence on a faithful 3D scan of the target object. Consumer scanning pipelines, such as depth cameras and photogrammetry, routinely introduce surface noise and scale errors that may not be apparent until print time. To evaluate whether AugPrint can still successfully print on top of low-fidelity meshes, we simulated errors in scanned meshes and checked the percentage of the print surface that would result in print-head collisions at different heights.

6.1 Corruption Model

We corrupt the reference mesh in two main ways: normal-direction noise and uniform scale error.

Normal-direction noise. To model surface-normal jitter from depth imaging, we displace each vertex along its outward normal. The displacement field is generated on a coarse 3D grid (cell size 20 mm) sampled from $\mathcal{N}(0, \sigma^2)$ and interpolated to each vertex, producing smooth, large-scale surface perturbations rather than per-vertex noise. We test three noise levels, with standard deviations $\sigma \in \{0.5, 1.0, 2.0\}$ mm.

Uniform scale error. Uncalibrated photogrammetry or incorrect unit assumptions produce systematic size errors. We

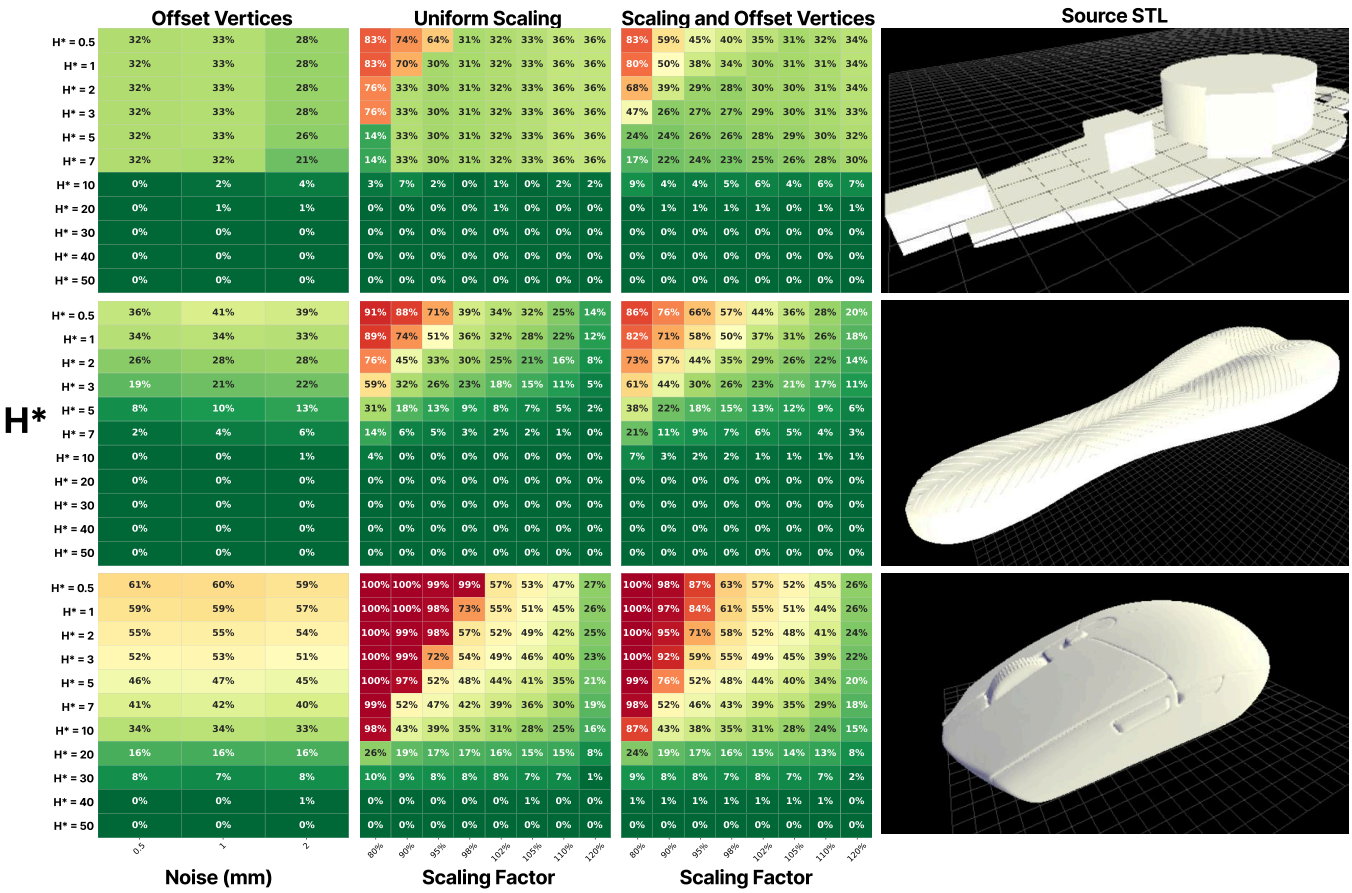


Figure 5: Print-head collision rates when trying to print with different H^* values. The toolpath is generated by using AugPrint's augmentation pipeline over a corrupted mesh. We test three separate types of mesh corruptions: 1) offset vertices, 2) uniform scaling, and 3) a combination of offset vertices with 2 mm noise and different uniform scaling values. These mimic common errors encountered during 3D object scanning.

scale the mesh uniformly about its centroid by factors in {80%, 90%, 95%, 98%, 102%, 105%, 110%, 120%}.

Combined corruption. We apply the highest noise level first (σ = 2 mm). Then, the resulting mesh is scaled. For a given trial of the experiment, we used the same normal-direction noise across all scale factors to isolate the effect of scale from noise variance.

6.2 Simulation Protocol

For each corrupted mesh, we ran AugPrint's slicer to generate a toolpath at the commanded standoff H^* over the corrupted surface estimate. We then simulate executing that toolpath over the original, unmodified mesh and determine whether a print-head collision (either with the print nozzle or the print-head body) would occur at each sampled point on the surface. We simulate print-head collisions based on the print-head dimensions of a Prusa MK4, the printer primarily used to print the demos shown in this paper.

We evaluate $H^* \in \{0.5, 1, 2, 3, 5, 7, 10, 20, 30, 40, 50\}$ across three objects spanning a range of surface geometries that we have used in our demos: a contoured bicycle seat, a computer mouse (Logitech G305), and a PCB. Stochastic conditions are averaged over five independent trials. We report the print-head collision rate.

6.3 Results

Figure 5 shows results. Here, we highlight some notable findings.

$H^* = 0.5$ *(traditional FFF,* $H = 0.2$ *mm).* Even at $\sigma = 0.5$ mm noise, well within the accuracy of consumer depth cameras, collision rates of 20–40% are observed. A 10% underestimate of object scale (90% factor) produces an 88% collision rate on the bike seat. Under combined corruption, rates exceed 80% for shrunken meshes. This highlights that traditional FFF 3D printing with stock printer configurations cannot reliably print on top of objects when relying on imprecise scanned meshes.

$H^* \geq 20$ *(*$H = 8$ *mm).* There are no collisions for either the PCB or bike seat, even with the combined simulated errors. An H^* of 20 corresponds to a print height of 8 mm. For VTP with NinjaFlex 85A TPU, this corresponds to a coil diameter of roughly 4 mm.

$H^* \geq 40$ *(*$H = 16$ *mm).* The highly contoured computer mouse required an H^* of 40 to avoid most print-head collisions with the

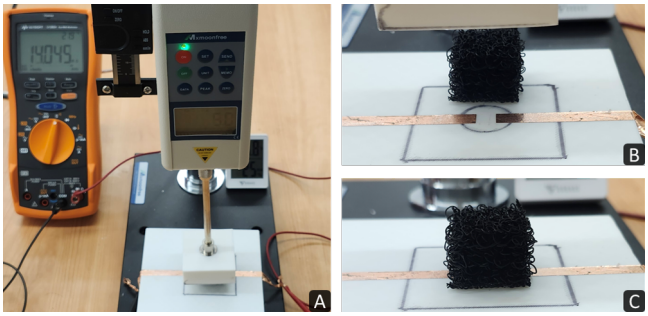


Figure 6: A) Conductive TPU pressure sensor testing apparatus. B) Gap between the copper tape. C) Foam pressure sensing cell bridging the copper tape gap.

corrupted meshes when only vertex noise or scaling factors were applied. An H^* of 40 corresponds to a print height of 16 mm and a coil diameter of roughly 8 mm. VTP still works with 8 mm coils, but the coarser deposition limits augmentation fidelity and could make it difficult to add textured surfaces to parts of the mouse. This simulation also assumes the full mouse is augmented; in practice, a user may only want to augment the regions where the palm rests, which would allow a significantly lower H^*.

VTP's tolerance to scan inaccuracy is a direct consequence of its elevated print height. As a starting point, we recommend $H^* \geq 10$ for gently curved objects with typical consumer scan quality (millimeter-level noise, scale error within ±10%), and $H^* \geq 20$ for extreme inaccuracies, such as poorly calibrated photogrammetry. Highly contoured objects require higher values; the mouse needed $H^* \geq 40$ to avoid most collisions. In practice, the minimum H^* computed during Upload and Analyze (Section 4.2) should be increased by a margin that reflects the expected scan error. Underestimating an object's size was among the most significant causes of print-head collisions, whereas small vertex displacements had little effect on the collision rate, likely because the toolpath was raised in some regions as often as it was lowered in others. The collision rate also understates the practical risk, since a single collision can cause a print to fail. With the mouse, for example, an H^* of 40 avoided 99% of collisions, but an H^* of 50 was needed to avoid all of them.

7 Pressure Sensing Characterization

A key advantage of VTP is that when printed with conductive elastomers, the resulting foam structures function as piezoresistive pressure sensors: compression brings conductive coils into closer contact, reducing electrical resistance. However, prior work on VTP sensors relied on specialized conductive TPE pellets (Shore 70A, volume resistivity of 10 Ω·cm) that are not readily available to everyday consumers [KRAIBURG TPE 2026] and demonstrated sensing only with unidirectional coil extrusion [Willemstein et al. 2025, 2024]. In this section, we show that pressure sensors can instead be fabricated using NinjaTek Eel, a conductive TPU filament readily available in the maker community, with a higher Shore hardness (90A) and higher volume resistivity (1500 Ω·cm). We also leverage a rectilinear VTP printing pattern, which crosshatches coils across layers, enabling more complex sensor geometries than prior work. To establish the viability of these sensors for the applications demonstrated in Section 8, we characterize their force-resistance response, hysteresis, recovery time, and print-to-print variability.

7.1 Experimental Setup

We printed $20 \times 20 \times 20$ mm conductive TPU foam cubes using VTP. Although the nominal dimensions were 20 mm per side, the coil structure at the edge marginally increases the actual dimensions. We measured the actual dimensions of each sample with calipers in full contact with the foam faces and used a precision balance to measure mass. For five foams printed with identical parameters, we computed the average density and used this value as the label for that printing condition. Compressive force was measured using a Mxmoonfree HP-500 force gauge (0.1 N resolution, ±0.5% accuracy, sampled at 10 Hz). Resistance was measured using a Keysight U1282A multimeter streaming real-time data at 16 Hz. Each sample was placed to bridge two strips of conductive copper tape (6.35 mm width, 7 mm apart) as shown in Figure 6.

7.2 Results

Our goal is to determine whether these sensors produce a signal that is reliable and responsive enough for the interactive applications in Section 8, where detecting the presence and relative magnitude of pressure matters more than precise force measurement. We focus on how the piezoresistive response varies with foam density, how hysteresis and recovery dynamics affect reuse at interactive rates, and how consistently the response reproduces across prints.

Force-Resistance Response. We characterized the relationship between applied compressive force and changes in resistance across foams of different densities. Using 5 N as a preload baseline (R_0), we report the resistance-change ratio $\Delta R/R_0$ at each load level (Figure 7). Prior to saturation, the magnitude of the resistance-change ratio decreases with increasing foam density, so denser foams respond more gradually to applied force. The 93.25 kg/m^3 foam, which we use in our applications, shows a clear monotonic response up to 50 N. We also measured compressive deformation under loads of 5, 10, 20, 50, and 100 N across five densities with three trials per density (Figure 7). Higher-density foams exhibit smaller deformations under identical loads, confirming that compressive stiffness increases with density.

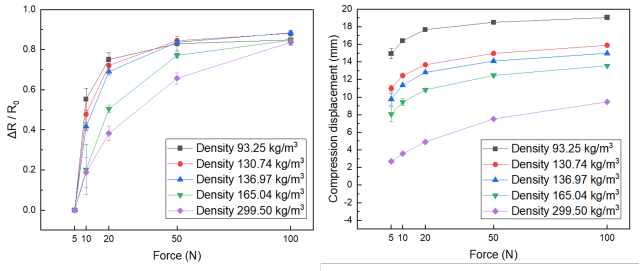


Figure 7: Different pressure sensors with their force-resistance curves and force-displacement curves.

Hysteresis. To characterize hysteresis, we tested a single 93.25 kg/m^3 specimen by stepping the load from 5 N through 10,

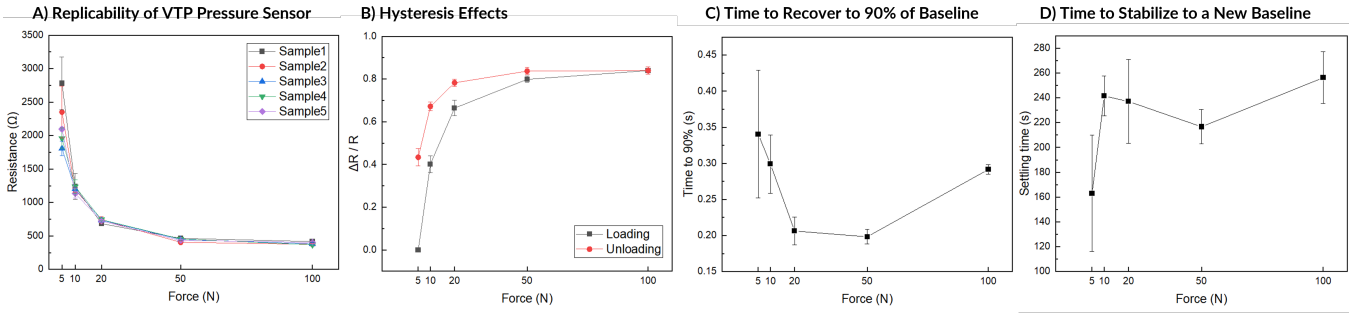


Figure 8: A) Force vs resistance plot showing the relatively low variance of VTP pressure sensor samples. B) The force-resistance hysteresis plot for a conductive TPU cube with a density of 93.25 kg/m^3. C) Recovery plot showing how long it takes to return to 90% of baseline. D) Stabilization plot showing how long sensors need to stabilize before no longer visibly changing values.

20, 50, and 100 N (holding at each level until the resistance stabilized), then stepping back down through the same levels. This sequence was repeated three times (Figure 8). We observe pronounced hysteresis during unloading: the resistance at a given force is consistently lower during unloading than during loading. For instance, the resistance at 20 N during unloading approximates the loading-phase resistance at 50 N. The foam also does not fully recover to its original loading resistance upon complete unloading. This behavior is consistent with viscoelastic recovery characteristics reported for VTP foams in prior work [Willemstein et al. 2025] and implies that applications requiring precise force measurement at low frequencies should account for directional drift. For applications demonstrated in Section 8, where we detect the presence and relative magnitude of pressure rather than exact force values, this level of hysteresis is acceptable.

Recovery and Stabilization Time. We tested how quickly a 93.25 kg/m^3 foam recovers after compression by measuring two quantities: (i) the time to recover to 90% of the pre-compression baseline resistance, and (ii) the time to reach a new stable baseline after release (Figure 8). The test was performed three times. The foams recovered to 90% of their baseline resistance within 0.2–0.35 seconds across all tested loads (5–100 N), indicating that the sensors can be reactuated at interactive rates without issue. However, full stabilization to a new baseline took substantially longer: approximately 160 seconds at 5 N and approximately 240 seconds at higher force levels. This means that for typical interactive use, where detecting the onset and relative magnitude of pressure is sufficient, the sensors respond quickly enough. Applications requiring precise measurement of low forces or true rest-state resistance would need to account for the longer stabilization period.

Print-to-Print Variability. Since the 93.25 kg/m^3 foam was selected for our application demonstrations, we evaluated the repeatability of its resistance-pressure response using five specimens printed with identical parameters (Figure 8). At low forces (5 N), the coefficient of variation across five prints reaches 17.37%, indicating significant measurement variability. However, at moderate to high forces, variability drops substantially: 3.51% at 10 N, 3.34% at 20 N, 5.27% at 50 N, and 5.29% at 100 N. Applications operating at low forces therefore benefit from per-sensor calibration, which our sensing circuit provides (Section 7.3).

7.3 Recognizing Gestures from Pressure Signals

We now extend our pressure-sensing characterization by investigating the feasibility of recognizing gestures from raw pressure signals to enable interactive experiences with augmented existing objects. Towards this end, we designed and printed a 3×3 pressure sensor array and used it for gesture recognition. The array consists of two layers of three parallel conductive foam channels, with the top-layer channels oriented orthogonally to the bottom-layer channels; their nine crossings form the 3×3 grid of sensing points.

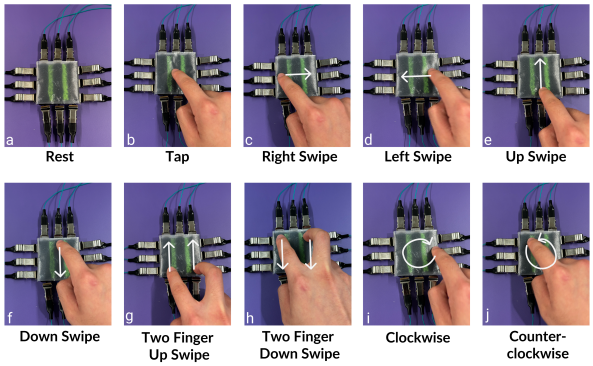


Figure 9: To enable interactive experiences with augmented objects, we demonstrate how the pressure signals derived from the augmentations can be used in a gestural interface. In this experiment, we evaluate the ability of a lightweight machine learning model to classify ten different gestures.

7.3.1 Circuit Design. Each foam sensor element is read using a Wheatstone bridge circuit, where the foam acts as a variable resistor whose resistance decreases under compression. An AD8421 instrumentation amplifier amplifies the bridge output, with gain adjustable via an MCP4662 digital potentiometer to accommodate foams of different baseline resistances. A CD74HC4067 multiplexer enables sequential polling of up to 16 sensors with a single circuit. To compensate for the variation in nominal resistance across foam elements described in our pressure sensing characterization, an additional MCP4662 is placed in series with each foam for per-sensor calibration, restoring bridge balance when unloaded. A Seeed XIAO

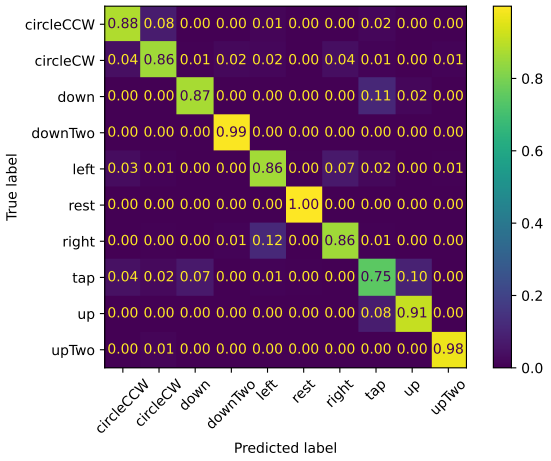


Figure 10: Confusion matrix for user-independent gesture recognition with our lightweight CNN-LSTM model (88.95% average accuracy).

ESP32-S3 microcontroller samples the conditioned voltage at 20 Hz and transmits data to a host via wired or wireless connection.

7.3.2 Gesture Recognition. To assess the potential of our pressure sensor array for interactive settings, we developed a machine-learning pipeline to detect gestures. We collected a dataset from six participants performing ten different gestures on the 3×3 pressure sensing array as seen in Figure 9. Participants were instructed to perform gestures at 1 Hz by following a metronome set to 60 BPM, and each gesture was performed 200 times, yielding a total dataset of 2000 gesture samples per participant.

Each sample consists of six voltage channels (one per foam channel and three per layer) sampled at 20 Hz. We trained a model consisting of a convolutional layer, a long short-term memory layer, and a fully connected layer, using leave-one-user-out cross-validation. In each fold, the model was trained on four participants, with one participant held out for validation and one for testing. Early stopping was employed to mitigate overfitting, terminating training when the validation loss did not decrease by more than 10^{-4} for 5 consecutive epochs; the test participant's data was never used during training or model selection.

The model achieved an average user-independent recognition accuracy of 88.95% across the ten gesture types (rest, tap, single-finger swipes, single-finger clockwise/counterclockwise motion, and two-finger down/up swipes), as seen in Figure 10. Classification errors occurred primarily between gestures with similar spatial footprints, e.g., taps versus short vertical swipes and left versus right swipes, and secondarily between clockwise and counterclockwise circles; increasing the number of sensing channels, and thus spatial resolution, would help disambiguate these cases.

7.4 Summary

These characterizations establish that conductive TPU foams printed with VTP using commercially available NinjaTek Eel filament are viable as embedded piezoresistive pressure sensors for interactive applications. The sensors exhibit a monotonic force-resistance response up to 50 N, recover to interactive-rate responsiveness within 0.35 seconds, and show consistent behavior across prints at forces at or above 10 N. Because the resistance response varies with foam density, sensor behavior can be tuned spatially through the same toolpath parameters that control stiffness.

8 End-to-End Applications

To demonstrate AugPrint's practical viability, we present several end-to-end applications that each leverage one or more system capabilities—direct-to-object printing, gradient density control, and embedded pressure sensing—to augment existing objects with soft, functional foam. Each application exercises a different subset of the design tool's features and targets a distinct use case. All artifacts were printed on an unmodified Prusa MK4 with a 0.4 mm nozzle, part-cooling fan disabled, and bed at 60 °C, inside an enclosure vented to the outdoors.

8.1 Gradient-Density Bike Seat with Pressure Mapping

Bike seats are a compelling target for AugPrint because they combine all three challenges the system addresses: the seat's curved geometry requires conformal deposition, rider comfort demands spatially varying stiffness, and pressure mapping requires embedded sensing.

We began by obtaining a smartphone scan of the bike seat and performing cleanup on the resulting mesh to remove scan artifacts, and then verifying that the mesh's overall dimensions roughly matched the physical object (e.g., the highest point on the mesh corresponded to the actual seat height). We then imported the mesh into the AugPrint design tool, selected the augmentation region, and applied a gradient density to create softer, more compliant regions where the rider's sit bones make contact, and firmer regions for lateral support.

Fabrication proceeded in several stages to integrate the pressure sensors. After printing the first VTP layer directly onto the bike seat, we attached copper tape contacts on top of this base layer to provide electrical connections for the sensors. We then printed several additional foam layers, paused the print to insert conductive TPU pressure sensor pads into cutouts in the foam, and printed two final layers on top to secure the sensors in place. The result is a custom-fit, gradient-density cushion with an embedded pressure sensor array that streams real-time pressure data, enabling the rider to visualize their weight distribution across the seat (Figure 11).

8.2 Creating Organizer Inserts

A useful property of VTP is that it self-stabilizes [Emery et al. 2024]: when printing at a fixed planar height above an object with varying surface geometry, coils deposited closer to the object are smaller and occupy less volume, while those farther from the object are larger. Over successive layers, this difference accumulates until the top surface reaches a uniform height, forming a flat plane regardless of the underlying geometry. We leverage this property to create tool inserts by printing with VTP in flat planes above an object and then flipping the part over (Figure 12). The resulting insert conforms to the tool's shape on one side and presents a flush, level

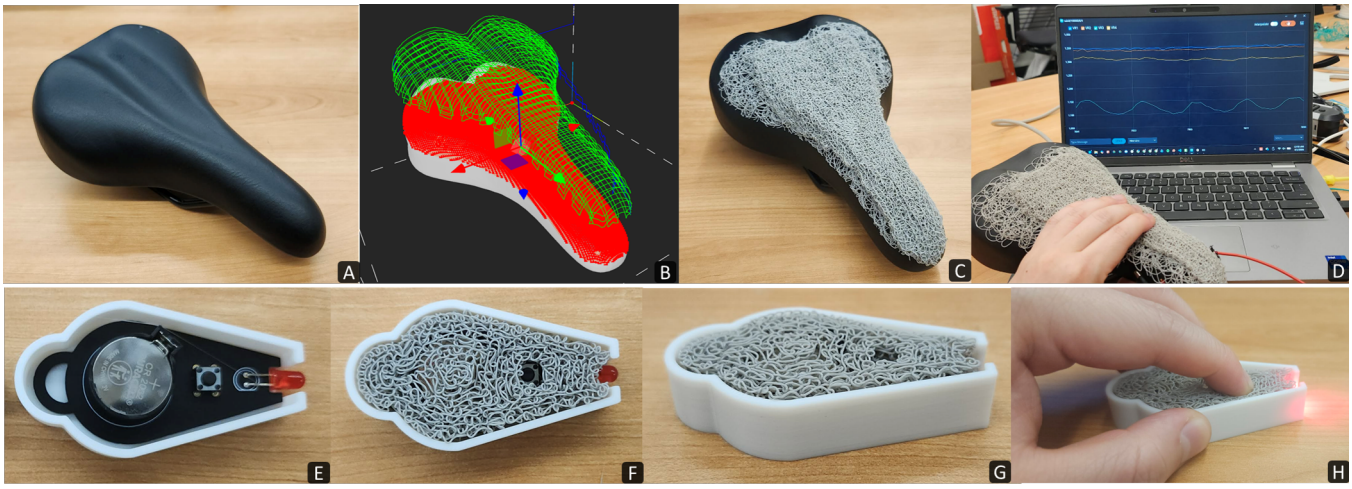


Figure 11: A) The original bike seat. B) The design tool interface showing our approach to augmenting it. C) The gradient density bike seat obtained from varying the print parameters. D) A user demonstrating the seat's pressure-sensing capabilities, pushing a portion of the seat cushion and observing the corresponding changes in the computer plot. E) The first half of the PCB enclosure. F) VTP augmentation inside the PCB enclosure shell to fill the gaps. G) A side view of the PCB enclosure showing a flush surface. H) Demonstrating how this approach allows continued usage of internal buttons.

surface on the other—all without requiring a mesh or any manual measurement.

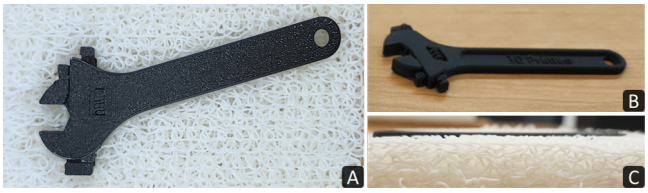


Figure 12: A) A tool organizer insert. B) The wrench printed on (H: 11 mm, L: 8.5 cm, W: 3.5 cm). C) Showing flush plane with wrench inserted.

8.3 Shock-Absorbing Microcontroller Enclosure

Designing enclosures for electronics typically requires precise CAD modeling to achieve a tight fit and a mechanism (e.g., snap clips or screws) to join the two halves. AugPrint simplifies this process by leveraging VTP's self-stabilization property [Emery et al. 2024] to fill voids around irregularly shaped components without requiring precise measurements (Figure 11).

We first created a rough 3D model of the PCB—intentionally low-fidelity, capturing only the overall dimensions and the locations of tall components. We then printed the base and walls of the enclosure using traditional FFF, placed the PCB inside, and extruded VTP foam to fill the remaining voids around the board. Because the VTP foam conforms to the PCB's geometry and self-stabilizes to a flat top surface, the enclosure achieves a snug fit without requiring precise internal dimensions. This approach could eliminate the need for a two-part enclosure design, enabling thinner walls since no space is required for joining mechanisms.

8.4 Input Controller

To show that we can support robust user interactions with AugPrint, we demonstrate how a pressure sensor array can enable quick input for games like Tetris (Figure 13). Our input latency for detecting a regional press is between 0.1 and 0.2 seconds.

We also show that we can use the controller for basic web browsing by mapping common touchpad gestures to the controller (e.g., a directional swipe to scroll, a clockwise swipe to refresh the page). Each gesture takes around one second to register.

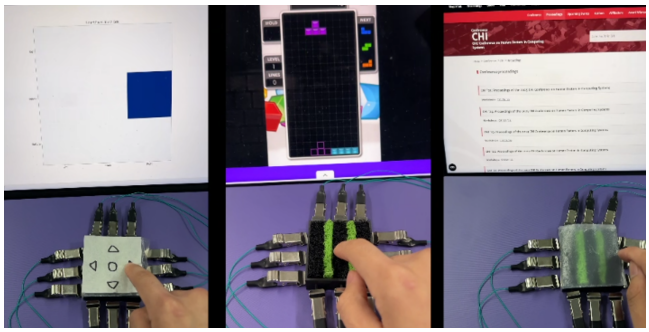


Figure 13: A controller to detect user input, either from pressing on a specific section of the surface to play Tetris or recognizing a swipe gesture to allow for basic web-browsing.

9 Discussion

AugPrint demonstrates that viscous thread printing can unify soft-structure fabrication, direct-to-object augmentation, and embedded interactivity using an unmodified consumer-grade 3D printer. While our end-to-end applications establish the practical viability of this approach, several limitations and opportunities for future work merit discussion.

Durability and Real-World Robustness. VTP foams exhibit weaker interlayer adhesion than solid prints, and this weakness is likely compounded at the high H^* values used for augmentation, where the extruded thread cools further before contacting the surface

below. Several strategies could improve durability. Printing within a heated enclosure would maintain filament temperature during deposition, improving interlayer adhesion at high H^* values. Post-print annealing could further strengthen the foam structure. For real-world deployment, a shell or fabric cover would likely be necessary to protect the porous foam from wear, grime buildup, and degradation. Such a cover could also serve as an attachment mechanism, securing the augmentation to the object without adhesives. Ensuring that augmentations remain fixed to objects under sustained use is an important engineering challenge that warrants further investigation.

Improving Generalizability. One way to broaden AugPrint's applicability is to leverage sensors already present on many consumer 3D printers—such as bed-leveling probes, extrusion flow sensors, and first-layer inspection cameras—to capture the surface geometry of objects placed on the build plate. This could eliminate the need for a separate scanning step to augment objects with VTP. Printer-side sensing could also be used to monitor VTP behavior in real time, enabling closed-loop calibration of VTP parameters for new materials without manual characterization.

Expanding the Material and Technique Space. Our demonstrations used PLA, NinjaFlex 85A TPU, and NinjaTek Eel conductive TPU. Expanding the palette of compatible materials would significantly broaden AugPrint's design space. Foaming TPUs, which contain blowing agents that release gas and expand the filament as it is extruded, could improve interlayer adhesion while also extending the range of achievable stiffnesses.

Characterizing Self-Stabilizing Behavior. While we demonstrated several practical uses of VTP's self-stabilizing behavior, fully characterizing the mechanism and predicting how many layers it takes for the layer height to stabilize is challenging and outside the scope of this paper. To characterize the self-stabilization mechanism, we would need to test different combinations of V^*, H^*, and ΔL across several types of geometries, with varying toolpathing. In this paper, we instead primarily focused on the novel idea of using VTP to directly print on top of existing objects, and we presented evaluations and demos highlighting the potential capabilities of VTP, even if it may require some trial and error to achieve the intended results. Community efforts around VTP characterization or sensorizing 3D printers to provide live feedback on VTP behavior would enable broader use of VTP for augmentation and reduce the trial-and-error currently required to apply VTP to new augmentation tasks.

Pressure Sensing Limitations. Our pressure sensing characterization (Section 7) focused primarily on foams at a single density (93.25 kg/m^3). While the force-resistance response, hysteresis, and recovery behavior we measured are promising for interactive applications, several limitations remain. The pronounced hysteresis and long full-stabilization time (approximately 240 seconds) make these sensors unsuitable for precise, low-frequency force measurement. The high coefficient of variation at low forces (17.37% at 5 N) suggests that per-sensor calibration is necessary for applications operating near the lower end of the sensing range. Future work should characterize a broader range of foam densities and explore whether alternative conductive filaments with lower volume resistivity could improve sensitivity and reduce variability.

10 Conclusion

We have presented AugPrint, a system for 3D printing soft foam augmentations directly onto existing curved objects using viscous thread printing and unmodified consumer-grade hardware. By leveraging viscous thread printing, AugPrint addresses the two persistent barriers to direct-to-object printing—imprecise surface meshes and print-head collisions—without requiring high-end scanners, multi-axis printers, or extended nozzles. Our computational design tool abstracts these fabrication constraints behind an interactive workflow supporting non-planar toolpath generation, gradient stiffness control, and surface texturing. We also demonstrated that commercially available conductive TPU can be used to create embedded piezoresistive pressure sensors within VTP foam, expanding beyond the inaccessible materials and unidirectional extrusion patterns of prior work. Our end-to-end applications illustrate that viscous thread printing can simultaneously enable conformal deposition, tunable compliance, and embedded sensing, allowing passive everyday objects to be retrofitted with soft, interactive interfaces on consumer hardware.

Acknowledgments

This work was funded by the Center for Research and Education on Accessible Technology and Experiences (CREATE) and NSF IIS 2327136. Jerry Cao was supported by the NSF GRFP under Grant No. DGE-2140004.

References

Jose Eduardo Aguilar-Segovia, Maxime Manzano, Sylvain Guégan, Ronan Le Breton, Alice Farhi-Rivasseau, and Sylvain Lefebvre. 2024. Multi-Material Torque Sensor Embedding One-Shot 3D-Printed Deformable Capacitive Structures. *IEEE Sensors Letters* 8, 9 (Aug. 2024), 2503204. doi:10.1109/LSENS.2024.3440195

Max Alberts, Troy Robert Nachtigall, Zjenja Doubrovski, and Daniel Saakes. 2024. From Dribbling Honey to Non-planar 3D-Printing: Coiling becomes Craft. In *Companion Publication of the 2024 ACM Designing Interactive Systems Conference*. Association for Computing Machinery, New York, NY, USA, 328–332. doi:10.1145/3656156.3665434

Ziyad Aloqalaa. 2022. Electrically Conductive Fused Deposition Modeling Filaments: Current Status and Medical Applications. *Crystals* 12, 8 (2022). doi:10.3390/cryst12081055

Daniel Ashbrook, Shitao Stan Guo, and Alan Lambie. 2016. Towards Augmented Fabrication: Combining Fabricated and Existing Objects. In *Proceedings of the 2016 CHI Conference Extended Abstracts on Human Factors in Computing Systems (CHI EA '16)*. Association for Computing Machinery, New York, NY, USA, 1510–1518. doi:10.1145/2851581.2892509

George Barnes and Richard Woodcock. 1958. Liquid Rope-Coil Effect. *Am. J. Phys.* 26, 4 (April 1958), 205–209. doi:10.1119/1.1996110

Jesse Burstyn, Nicholas Fellion, Paul Strohmeier, and Roel Vertegaal. 2015. PrintPut: Resistive and Capacitive Input Widgets for Interactive 3D Prints. In *Human-Computer Interaction – INTERACT 2015 (Lecture Notes in Computer Science)*. Springer, Cham, 332–339. doi:10.1007/978-3-319-22701-6_25

Jerry Cao, Yuecheng Peng, Hongrui Wu, Yuxuan Miao, Sanjana Satagopan, Runxin Shi, Brier Hehmeyer, Brett Emery, Jeffrey Lipton, Jennifer Mankoff, and Shwetak Naran Patel. 2026. Demonstrating SensiPrint: 3D-Printed Soft Foams for Physical Augmentation and Sensing. In *Adjunct Proceedings of the 10th ACM Symposium on Computational Fabrication* (Cambridge, MA, USA) *(SCF Adjunct '25)*. Association for Computing Machinery, New York, NY, USA, Article 14, 3 pages. doi:10.1145/3774746.3779262

Xiang 'Anthony' Chen, Stelian Coros, and Scott E. Hudson. 2018. Medley: A Library of Embeddables to Explore Rich Material Properties for 3D Printed Objects. In *Proceedings of the 2018 CHI Conference on Human Factors in Computing Systems (CHI '18)*. Association for Computing Machinery, New York, NY, USA, 1–12. doi:10.1145/3173574.3173736

Xiang 'Anthony' Chen, Stelian Coros, Jennifer Mankoff, and Scott E. Hudson. 2015. Encore: 3D Printed Augmentation of Everyday Objects with Printed-Over, Affixed and Interlocked Attachments. In *Proceedings of the 28th Annual ACM Symposium on User Interface Software & Technology (UIST '15)*. Association for Computing Machinery, New York, NY, USA, 73–82. doi:10.1145/2807442.2807498

Xiang 'Anthony' Chen, Jeeeun Kim, Jennifer Mankoff, Tovi Grossman, Stelian Coros, and Scott E. Hudson. 2016. Reprise: A Design Tool for Specifying, Generating, and Customizing 3D Printable Adaptations on Everyday Objects. In *Proceedings of the 29th Annual ACM Symposium on User Interface Software and Technology*. Association for Computing Machinery, New York, NY, USA, 29–39. doi:10.1145/2984511.2984512

Oliver Child, Ollie Hanton, Jack Dawson, Steve Hodges, and Mike Fraser. 2026. Printegrated Circuits: Personal Fabrication of 3D Printed Devices with Embedded PCBs. In *Proceedings of the Twentieth International Conference on Tangible, Embedded, and Embodied Interaction (TEI '26)*. Association for Computing Machinery, New York, NY, USA, 1–19. doi:10.1145/3731459.3773307

Chen Chu, Greg Graf, and David W. Rosen. 2008. Design for Additive Manufacturing of Cellular Structures. *Computer-Aided Design and Applications* 5, 5 (Jan. 2008), 686–696. doi:10.3722/cadaps.2008.686-696

Francesco Di Stefano, Alban Gorreja, Mattia Balestra, and Roberto Pierdicca. 2021. Mobile 3D scan LiDAR: a literature review. *Geomatics, Natural Hazards and Risk* 12 (2021), 2387–2429. doi:10.1080/19475705.2021.1964617

B. Emery, D. L. Revier, and J. I. Lipton. 2021. Applied Viscous Thread Instability for Manufacturing 3D Printed Foams. In *Proceedings of the 2021 International Solid Freeform Fabrication Symposium*. University of Texas at Austin, Austin, TX, USA. doi:10.26153/tsw/17490

Brett Emery, Kelsey L. Snapp, Daniel Revier, Vivek Sarkar, Masa Nakura, Keith A. Brown, and Jeffrey Ian Lipton. 2024. Foams with 3D Spatially Programmed Mechanics Enabled by Autonomous Active Learning on Viscous Thread Printing. *Advanced Science* 11, 44 (Nov. 2024), 2408062. doi:10.1002/advs.202408062

Sean Follmer, David Carr, Emily Lovell, and Hiroshi Ishii. 2010. CopyCAD: remixing physical objects with copy and paste from the real world. In *Adjunct Proceedings of the 23rd Annual ACM Symposium on User Interface Software and Technology*. Association for Computing Machinery, New York, NY, USA, 381–382. doi:10.1145/1866218.1866230

Aref Ghorbani, Sophia Jennie Giancoli, Seyed Ali Ghoreishy, Martijn Noort, and Mehdi Habibi. 2024. A novel 3D food printing technique: achieving tunable porosity and fracture properties via liquid rope coiling. *ArXiv e-prints* (Sept. 2024). doi:10.48550/arXiv.2409.01487 arXiv:2409.01487

Ian Gibson, David Rosen, Brent Stucker, and Amirmahyar Khorasani. 2020. *Additive Manufacturing Technologies*. Springer, Cham. doi:10.1007/978-3-030-56127-7

Jun Gong, Olivia Seow, Cedric Honnet, Jack Forman, and Stefanie Mueller. 2021. MetaSense: Integrating Sensing Capabilities into Mechanical Metamaterial. In *Proceedings of the 34th Annual ACM Symposium on User Interface Software and Technology*. Association for Computing Machinery, New York, NY, USA, 1063–1073. doi:10.1145/3472749.3474806

Jaime Gould, Camila Friedman-Gerlicz, and Leah Buechley. 2024. TRAvel Slicer: Continuous Extrusion Toolpaths for 3D Printing. In *Proceedings of the 37th Annual ACM Symposium on User Interface Software and Technology (UIST '24)*. Association for Computing Machinery, New York, NY, USA, Article 122, 17 pages. doi:10.1145/3654777.3676349

Ben Greenspan, Eric Gallo, and Andreea Danielescu. 2022. FlexKeys: Rapidly Customizable 3D Printed Tactile Input Devices with No Assembly Required. In *Additive Manufacturing, Modeling Systems and 3D Prototyping*, Vol. 34. AHFE Open Access. doi:10.54941/ahfe1001587

Rafael Guerra Silva, Cristóbal Salinas Estay, Gustavo Morales Pavez, Jorge Zahr Viñuela, and María Josefina Torres. 2021. Influence of Geometric and Manufacturing Parameters on the Compressive Behavior of 3D Printed Polymer Lattice Structures. *Materials* 14, 6 (2021), 1462. doi:10.3390/ma14061462

Anhong Guo, Jeeeun Kim, Xiang 'Anthony' Chen, Tom Yeh, Scott E. Hudson, Jennifer Mankoff, and Jeffrey P. Bigham. 2017. Facade: Auto-generating Tactile Interfaces to Appliances. In *Proceedings of the 2017 CHI Conference on Human Factors in Computing Systems*. Association for Computing Machinery, New York, NY, USA, 5826–5838. doi:10.1145/3025453.3025845

Mehdi Habibi, Maniya Maleki, Ramin Golestanian, Neil M. Ribe, and Daniel Bonn. 2006. Dynamics of liquid rope coiling. *Phys. Rev. E* 74, 6 (Dec. 2006), 066306. doi:10.1103/PhysRevE.74.066306

Liang He, Jarrid A. Wittkopf, Ji Won Jun, Kris Erickson, and Rafael Tico Ballagas. 2021. ModElec: A Design Tool for Prototyping Physical Computing Devices Using Conductive 3D Printing. *Proceedings of the ACM on Interactive, Mobile, Wearable and Ubiquitous Technologies* 5, 4 (Dec. 2021), 1–20. doi:10.1145/3495000

Kunihiro Kato, Kaori Ikematsu, and Yoshihiro Kawahara. 2020. CAPath: 3D-Printed Interfaces with Conductive Points in Grid Layout to Extend Capacitive Touch Inputs. *Proceedings of the ACM on Human-Computer Interaction* 4, ISS (Nov. 2020), 1–17. doi:10.1145/3427321

John Klein, Michael Stern, Giorgia Franchin, Markus Kayser, Chikara Inamura, Shreya Dave, James C. Weaver, Peter Houk, Paolo Colombo, Maria Yang, and Neri Oxman. 2015. Additive Manufacturing of Optically Transparent Glass. *3D Printing and Additive Manufacturing* 2, 3 (Sept. 2015), 92–105. doi:10.1089/3dp.2015.0021

Yuki Koyama, Shinjiro Sueda, Emma Steinhardt, Takeo Igarashi, Ariel Shamir, and Wojciech Matusik. 2015. AutoConnect: computational design of 3D-printable connectors. *ACM Trans. Graph.* 34, 6 (2015), 231:1–231:11. doi:10.1145/2816795.2818060

KRAIBURG TPE. 2026. THERMOLAST® K TC7OEX-BLCK (Series: EC) Datasheet. UL Prospector. https://www.ulprospector.com/plastics/en/datasheet/431992/thermolast-k-tc7oex-blck-series-ec Accessed March 29, 2026.

Hsuanling Lee, Yujie Shan, Huachao Mao, and Liang He. 2024. Fluxable: A Tool for Making 3D Printable Sensors and Actuators. In *Adjunct Proceedings of the 37th Annual ACM Symposium on User Interface Software and Technology*. Association for Computing Machinery, New York, NY, USA, 1–3. doi:10.1145/3672539.3686342

Jiahao Li, Jeeeun Kim, and Xiang 'Anthony' Chen. 2019. Robiot: A Design Tool for Actuating Everyday Objects with Automatically Generated 3D Printable Mechanisms. In *Proceedings of the 32nd Annual ACM Symposium on User Interface Software and Technology (UIST '19)*. Association for Computing Machinery, New York, NY, USA, 673–685. doi:10.1145/3332165.3347894

Jiahao Li, Alexis Samoylov, Jeeeun Kim, and Xiang 'Anthony' Chen. 2022. Roman: Making Everyday Objects Robotically Manipulable with 3D-Printable Add-on Mechanisms. In *Proceedings of the 2022 CHI Conference on Human Factors in Computing Systems (CHI '22)*. Association for Computing Machinery, New York, NY, USA, 1–17. doi:10.1145/3491102.3501818

Jeffrey I. Lipton and Hod Lipson. 2016. 3D Printing Variable Stiffness Foams Using Viscous Thread Instability. *Sci. Rep.* 6, 29996 (Aug. 2016), 1–6. doi:10.1038/srep29996

Hao Liu, Zhoupeng Liu, and Siting Hao. 2021. Design of a Throat-extended FDM Extruder for Multi-axis 3D Printing. *Strojniški vestnik - Journal of Mechanical Engineering* 67, 4 (2021), 180–190. doi:10.5545/sv-jme.2021.7124

Dingyifei Ma, Xiaoqing Tian, Jiang Han, and Lian Xia. 2023. Modeling for silicone foam material extrusion with liquid rope coiling. *Int. J. Mech. Sci.* 249 (July 2023), 108234. doi:10.1016/j.ijmecsci.2023.108234

M. Maleki, M. Habibi, R. Golestanian, N. M. Ribe, and Daniel Bonn. 2004. Liquid Rope Coiling on a Solid Surface. *Phys. Rev. Lett.* 93, 21 (Nov. 2004), 214502. doi:10.1103/PhysRevLett.93.214502

Maryam Mansoori, Negar Kalantar, and William Palmer. 2018. *Handmade by Machine: A Study on Layered Paste Deposition Methods in 3D Printing Geometric Sculptures*. https://www.researchgate.net/publication/327212191

Karola Marky, Martin Schmitz, Verena Zimmermann, Martin Herbers, Kai Kunze, and Max Mühlhäuser. 2020. 3D-Auth: Two-Factor Authentication with Personalized 3D-Printed Items. In *Proceedings of the 2020 CHI Conference on Human Factors in Computing Systems*. Association for Computing Machinery, New York, NY, USA, 1–12. doi:10.1145/3313831.3376189

Jonàs Martínez, Jérémie Dumas, and Sylvain Lefebvre. 2016. Procedural voronoi foams for additive manufacturing. *ACM Trans. Graph.* 35, 4 (July 2016), 44:1–44:12. doi:10.1145/2897824.2925922

Jacob N. Miske, Brett A. Emery, Keith A. Brown, and Jeffrey I. Lipton. 2025. Compression, Shear, and Flexural Durability of Viscous Thread Printed (VTP) Foams Produced from Thermoplastic Polyurethane for Consumer Goods. In *Proceedings of the 2025 International Solid Freeform Fabrication Symposium*. University of Texas at Austin, Austin, TX, USA. doi:10.26153/tsw/63393

Stefanie Mueller, Tobias Mohr, Kerstin Guenther, Johannes Frohnhofen, and Patrick Baudisch. 2014. faBrickation: fast 3D printing of functional objects by integrating construction kit building blocks. In *Proceedings of the SIGCHI Conference on Human Factors in Computing Systems*. ACM, New York, NY, USA, 3827–3834. doi:10.1145/2556288.2557005

Joseph T. Muth, Patrick G. Dixon, Logan Woish, Lorna J. Gibson, and Jennifer A. Lewis. 2017. Architected cellular ceramics with tailored stiffness via direct foam writing. *Proceedings of the National Academy of Sciences of the United States of America* 114, 8 (Feb. 2017), 1832–1837. doi:10.1073/pnas.1616769114

Masa Nakura, Vivek Sarkar, Daniel Revier, Brett Emery, and Jeffrey I. Lipton. 2024. An Interpolative Slicing Algorithm for Continuously Graded Stiffness in Viscous Thread Printed Foams. In *Proceedings of the 2024 International Solid Freeform Fabrication Symposium*. University of Texas at Austin, Austin, TX, USA. doi:10.26153/tsw/58279

Mohammadreza Nofar, Julia Utz, Nico Geis, Volker Altstädt, and Holger Ruckdäschel. 2022. Foam 3D Printing of Thermoplastics: A Symbiosis of Additive Manufacturing and Foaming Technology. *Advanced Science* 9, 11 (2022), 2105701. doi:10.1002/advs.202105701

Doga Ozbek, Marwa Alalawi, Till Max Eckroth, and Michael Wessely. 2024. Demonstration of AcceloPrint: Fabricating Accelerometers with Multi-Material 3D Printing. In *Adjunct Proceedings of the 9th ACM Symposium on Computational Fabrication (SCF Adjunct '24)*. Association for Computing Machinery, New York, NY, USA, 1–3. doi:10.1145/3665662.3673256

Doga Ozbek, Marwa AlAlawi, and Michael Wessely. 2025. AcceloPrint: Fabricating Customizable Accelerometers with Multi-Material 3D Printing. In *Proceedings of the Extended Abstracts of the CHI Conference on Human Factors in Computing Systems (CHI EA '25)*. Association for Computing Machinery, New York, NY, USA, 1–8. doi:10.1145/3706599.3720059

Huaishu Peng, Jimmy Briggs, Cheng-Yao Wang, Kevin Guo, Joseph Kider, Stefanie Mueller, Patrick Baudisch, and François Guimbretière. 2018. RoMA: Interactive Fabrication with Augmented Reality and a Robotic 3D Printer. In *Proceedings of the 2018 CHI Conference on Human Factors in Computing Systems (CHI '18)*. Association for Computing Machinery, New York, NY, USA, 1–12. doi:10.1145/3173574.3174153

Mayur Jiyalal Prajapati, Chinmai Bhat, Ajeet Kumar, Saurav Verma, Shang-Chih Lin, and Jeng-Ywan Jeng. 2022. Supportless Lattice Structure for Additive Manufacturing of Functional Products and the Evaluation of Its Mechanical Property at Variable Strain Rates. *Materials* 15, 22 (2022). doi:10.3390/ma15227954

Raf Ramakers, Fraser Anderson, Tovi Grossman, and George Fitzmaurice. 2016. RetroFab: A Design Tool for Retrofitting Physical Interfaces using Actuators, Sensors and 3D Printing. In *Proceedings of the 2016 CHI Conference on Human Factors in Computing Systems (CHI '16)*. Association for Computing Machinery, New York, NY, USA, 409–419. doi:10.1145/2858036.2858485

N. M. Ribe. 2004. Coiling of viscous jets. *Proc. R. Soc. Lond. A.* 460, 2051 (Nov. 2004), 3223–3239. doi:10.1098/rspa.2004.1353

Neil M. Ribe, Mehdi Habibi, and Daniel Bonn. 2012. Liquid Rope Coiling. *Annu. Rev. Fluid Mech.* 44 (Jan. 2012), 249–266. doi:10.1146/annurev-fluid-120710-101244

Laura Robles-Lorite, Alberto García-Collado, Eloísa Torres-Jiménez, and Rubén Dorado-Vicente. 2025. Tolerance of lattice struts manufactured without supports via fused filament fabrication. *The International Journal of Advanced Manufacturing Technology* 139, 3 (2025), 1933–1944. doi:10.1007/s00170-025-16003-x

Rei Sakura, Changyo Han, Yahui Lyu, Keisuke Watanabe, Ryosuke Yamamura, and Yasuaki Kakehi. 2023. LattiSense: A 3D-Printable Resistive Deformation Sensor with Lattice Structures. In *Proceedings of the 8th ACM Symposium on Computational Fabrication (SCF '23)*. Association for Computing Machinery, New York, NY, USA, 1–14. doi:10.1145/3623263.3623361

Rei Sakura, Changyo Han, Keisuke Watanabe, Ryosuke Yamamura, and Yasuaki Kakehi. 2022. Design of 3D-Printed Soft Sensors for Wire Management and Customized Softness. In *Extended Abstracts of the 2022 CHI Conference on Human Factors in Computing Systems (CHI EA '22)*. Association for Computing Machinery, New York, NY, USA, 1–5. doi:10.1145/3491101.3519906

Rei Sakura and Yasuaki Kakehi. 2025. A 3D-Printed Touch Sensor with a Single-Stroke Conductive Path. In *Proceedings of the Extended Abstracts of the CHI Conference on Human Factors in Computing Systems (CHI EA '25)*. Association for Computing Machinery, New York, NY, USA, 1–6. doi:10.1145/3706599.3720023

Valkyrie Savage, Ryan Schmidt, Tovi Grossman, George Fitzmaurice, and Björn Hartmann. 2014. A series of tubes: adding interactivity to 3D prints using internal pipes. In *Proceedings of the 27th Annual ACM Symposium on User Interface Software and Technology*. Association for Computing Machinery, New York, NY, USA, 3–12. doi:10.1145/2642918.2647374

Valkyrie Savage, Xiaohan Zhang, and Björn Hartmann. 2012. Midas: fabricating custom capacitive touch sensors to prototype interactive objects. In *Proceedings of the 25th Annual ACM Symposium on User Interface Software and Technology*. Association for Computing Machinery, New York, NY, USA, 579–588. doi:10.1145/2380116.2380189

Martin Schmitz, Martin Herbers, Niloofar Dezfuli, Sebastian Günther, and Max Mühlhäuser. 2018. Off-Line Sensing: Memorizing Interactions in Passive 3D-Printed Objects. In *Proceedings of the 2018 CHI Conference on Human Factors in Computing Systems*. Association for Computing Machinery, New York, NY, USA, 1–8. doi:10.1145/3173574.3173756

Martin Schmitz, Mohammadreza Khalilbeigi, Matthias Balwierz, Roman Lissermann, Max Mühlhäuser, and Jürgen Steimle. 2015. Capricate: A Fabrication Pipeline to Design and 3D Print Capacitive Touch Sensors for Interactive Objects. In *Proceedings of the 28th Annual ACM Symposium on User Interface Software and Technology*. Association for Computing Machinery, New York, NY, USA, 253–258. doi:10.1145/2807442.2807503

Martin Schmitz, Florian Müller, Max Mühlhäuser, Jan Riemann, and Huy Viet Viet Le. 2021. Itsy-Bits: Fabrication and Recognition of 3D-Printed Tangibles with Small Footprints on Capacitive Touchscreens. In *Proceedings of the 2021 CHI Conference on Human Factors in Computing Systems*. Association for Computing Machinery, New York, NY, USA, 1–12. doi:10.1145/3411764.3445502

Martin Schmitz, Jürgen Steimle, Jochen Huber, Niloofar Dezfuli, and Max Mühlhäuser. 2017. Flexibles: Deformation-Aware 3D-Printed Tangibles for Capacitive Touchscreens. In *Proceedings of the 2017 CHI Conference on Human Factors in Computing Systems*. Association for Computing Machinery, New York, NY, USA, 1001–1014. doi:10.1145/3025453.3025663

Michael S. Silverstein. 2014. PolyHIPEs: Recent advances in emulsion-templated porous polymers. *Progress in Polymer Science* 39, 1 (Jan. 2014), 199–234. doi:10.1016/j.progpolymsci.2013.07.003

Blair Subbaraman, Nathaneal Bursch, and Nadya Peek. 2025. It's Not the Shape, It's the Settings: Tools for Exploring, Documenting, and Sharing Physical Fabrication Parameters in 3D Printing. In *Proceedings of the 2025 CHI Conference on Human Factors in Computing Systems (CHI '25)*. Association for Computing Machinery, New York, NY, USA, 1–19. doi:10.1145/3706598.3713354

Blair Subbaraman and Nadya Peek. 2024. Playing the Print: MIDI-Based Fabrication Interfaces to Explore and Document Material Behavior. In *Extended Abstracts of the CHI Conference on Human Factors in Computing Systems (CHI EA '24)*. Association for Computing Machinery, New York, NY, USA, 1–8. doi:10.1145/3613905.3650966

Lingyun Sun, Yue Yang, Yu Chen, Jiaji Li, Danli Luo, Haolin Liu, Lining Yao, Ye Tao, and Guanyun Wang. 2021. ShrinCage: 4D Printing Accessories that Self-Adapt. In *Proceedings of the 2021 CHI Conference on Human Factors in Computing Systems (CHI '21)*. Association for Computing Machinery, New York, NY, USA, 1–12. doi:10.1145/3411764.3445220

Haruki Takahashi and Homei Miyashita. 2017. Expressive Fused Deposition Modeling by Controlling Extruder Height and Extrusion Amount. In *Proceedings of the 2017 CHI Conference on Human Factors in Computing Systems (CHI '17)*. Association for Computing Machinery, New York, NY, USA, 5065–5074. doi:10.1145/3025453.3025933

Alexander Teibrich, Stefanie Mueller, François Guimbretière, Robert Kovacs, Stefan Neubert, and Patrick Baudisch. 2015. Patching Physical Objects. In *Proceedings of the 28th Annual ACM Symposium on User Interface Software & Technology (UIST '15)*. Association for Computing Machinery, New York, NY, USA, 83–91. doi:10.1145/2807442.2807467

Xiaoqing Tian, Jeffery Plott, Hongjun Wang, Bizhong Zhu, and Albert J. Shih. 2017. Silicone Foam Additive Manufacturing by Liquid Rope Coiling. *Procedia CIRP* 65 (Jan. 2017), 196–201. doi:10.1016/j.procir.2017.04.050

Nobuyuki Umetani and Ryan Schmidt. 2017. SurfCuit: Surface-Mounted Circuits on 3D Prints. *IEEE Computer Graphics and Applications* 38, 3 (May 2017), 52–60. doi:10.1109/MCG.2017.40

Claas Willem Visser, Dahlia N. Amato, Jochen Mueller, and Jennifer A. Lewis. 2019. Architected Polymer Foams via Direct Bubble Writing. *Advanced Materials* 31, 46 (2019), 1904668. doi:10.1002/adma.201904668

Ludwig Wilhelm Wall, Alec Jacobson, Daniel Vogel, and Oliver Schneider. 2021. Scrappy: Using Scrap Material as Infill to Make Fabrication More Sustainable. In *Proceedings of the 2021 CHI Conference on Human Factors in Computing Systems (CHI '21)*. Association for Computing Machinery, New York, NY, USA, 1–12. doi:10.1145/3411764.3445187

Ludwig Wilhelm Wall, Oliver Schneider, and Daniel Vogel. 2023. Substiports: User-Inserted Ad Hoc Objects as Reusable Structural Support for Unmodified FDM 3D Printers. In *Proceedings of the 36th Annual ACM Symposium on User Interface Software and Technology (UIST '23)*. Association for Computing Machinery, New York, NY, USA, 1–20. doi:10.1145/3586183.3606718

Guanyun Wang, Haotian Chen, Yufeng Wang, Songyun Li, Yue Tao, Fanke Qi, Lizhuo Cao, Xiao Jin, Ye Tao, and Jiaji Li. 2025. GyFoam: Fabricating Lattice Foam with Customizable Stiffness through Uniform Expansion. In *Proceedings of the 38th Annual ACM Symposium on User Interface Software and Technology (UIST '25)*. Association for Computing Machinery, New York, NY, USA, 1–16. doi:10.1145/3746059.3747785

Christian Weichel, John Hardy, Jason Alexander, and Hans Gellersen. 2015. ReForm: Integrating Physical and Digital Design through Bidirectional Fabrication. In *Proceedings of the 28th Annual ACM Symposium on User Interface Software and Technology*. Association for Computing Machinery, New York, NY, USA, 93–102. doi:10.1145/2807442.2807451

Michael Wessely, Ticha Sethapakdi, Carlos Castillo, Jackson C. Snowden, Ollie Hanton, Isabel P. S. Qamar, Mike Fraser, Anne Roudaut, and Stefanie Mueller. 2020. Sprayable User Interfaces: Prototyping Large-Scale Interactive Surfaces with Sensors and Displays. In *Proceedings of the 2020 CHI Conference on Human Factors in Computing Systems*. Association for Computing Machinery, New York, NY, USA, 1–12. doi:10.1145/3313831.3376249

Nick Willemstein, Saivimal Sridar, Herman van der Kooij, and Ali Sadeghi. 2025. A feasibility study on using soft insoles for estimating 3D ground reaction forces with incorporated 3D-printed foam-like sensors. *Wearable Technologies* 6 (Jan. 2025), e3. doi:10.1017/wtc.2024.23

Nick Willemstein, Herman van der Kooij, and Ali Sadeghi. 2024. 3D-Printed Soft Proprioceptive Graded Porous Actuators with Strain Estimation by System Identification. *Advanced Intelligent Systems* 6, 9 (2024), 2300890. doi:10.1002/aisy.202300890